A Ray Tracing Tool for Propagation Modeling in Layered Media: A Case Study at the Chip Scale

FRANCO FUSCHINI [1], **MARINA BARBIROLI** [1], **GAETANO BELLANCA** [2], **GIOVANNA CALÒ** [3] (Member, IEEE), **JACOPO NANNI** [1], **AND VINCENZO PETRUZZELLI** [3]

[1] Department of Electrical, Electronic and Information Engineering "G. Marconi," University of Bologna, 40136 Bologna, Italy

[2] Department of Engineering, University of Ferrara, 44124 Ferrara, Italy

[3] Department of Electrical and Information Engineering, Polytechnic University of Bari, 70126 Bari, Italy

CORRESPONDING AUTHOR: F. FUSCHINI (e-mail: franco.fuschini@unibo.it)

ABSTRACT Nowadays, many wireless applications require the exchange of electromagnetic waves through propagation environments that look like to stratified media to some extent. This may concern both natural scenarios, e.g., air/vegetation/ground, and artificial structures, like meta-materials, photonic devices, solar cells or systems-on-chip. The characterization of the layered propagation channel is therefore important for the design and deployment of effective devices and systems. To this aim, the Dyadic Green Function method has been often leveraged, although its use is usually limited to simple sources, like short dipoles or current elements. Furthermore, it seems unsuited to assess the dispersive properties of the channel, which are known to become important when high data-rate must be conveyed. In this paper, a ray-based approach to propagation inside layers is proposed. As the layered environment can be quite reverberating, a great number of rays may be needed, to the extent that the corresponding computational burden might be hardly afforded by general purpose ray tracing tools. Therefore, the ray tracing engine here presented is specifically conceived for the layered case, and mostly relies on analytical formulation. The accuracy of the model is checked against measurement carried out at chip scale at optical frequency, as a reference study case.

INDEX TERMS Electromagnetic propagation, layered media, ray tracing, system-on-chip, wireless communications.

I. INTRODUCTION

THE RESTLESS increase in communication systems deployment to comply with a rising number of services and applications with different Quality of Services requirements has spurred the development of a large number of prediction methodologies and mathematical tools for reliable system design. It is well known that propagation modeling plays a key role in wireless network planning, especially in challenging contexts, e.g., when indoor coverage from an outdoor Base Station is required, when higher frequencies such as millimeter waves are exploited, or in Wireless Networks On Chip (WiNoC) for chip-scale connectivity, where many cores are integrated on the same chip to comply with the endless request of increased computing capabilities.

WiNoCs have been proposed as an alternative paradigm for the communication between different chips and, in most advanced proposals, between different cores [1] on the same chip; the possibility of removing the intricacy and overhead of a wired network topology is indeed a great advantage of wireless communication. However, unless very high frequencies are envisaged, such networks are limited by the size of the antennas and, consequently, by the chip area usage. In this regard, optical wireless interconnects may represent a breakthrough, overcoming the bottleneck of both wired interconnects and WiNoCs at lower frequencies [2].

According to the schematic representation of an integrated circuit [3], propagation in a layered medium has to be investigated and modeled for WiNoC design. In

TABLE 1. DGF vs RT models.

	Field computation	Antenna type	Materials	Computation effort
DGF	• Near- and far-field • Mainly limited to the total field, no easy way to address signal spread in the time/frequency/angular domain	Short electric dipoles / current elements	Lossless and lossy	Not always reliable with many layers / at high frequencies / if the antennas are not in the same layer [18]
RT	• Far-field; • Inherently fit to track the multipath nature of propagation	Any radiation pattern can be more easily taken into account	Lossless	Tolerable effort up to distances much greater than λ (especially true for the RT tool here presented owing to its analytical formulation)

spite of the previous studies investigating the properties of the on-chip wireless layered channel [2], [5]–[8], [22], its characterization is still incomplete [4].

Propagation in regions with different electromagnetic characteristics, bounded by flat or rough surfaces has been widely investigated also in different domains, starting from Sommerfield's studies [9] and then extended to the two-layers case and the multi-layered case, as summarized in [10]. Propagation in layered media has been often related to Extremely Low Frequency communications for subsurface and close-to-the-surface communications, geophysical prospecting and diagnostics [11], to radio-wave propagation for VHF/UHF links in environment where the layers represent ground, vegetation or snow-covered terrain and air [12]. Other fields of application include propagation in meta-materials, photonics crystals, solar cells and plasmonic devices [13], ultrasonic testing in geometrically complex structures like anisotropic, inhomogeneous materials [14], earthquake location in geophysics, migration imaging and travel time tomography [15].

According to a literature survey, propagation modelling in layered structures can be carried out according to some, different methodologies, spanning Sommerfeld integration methods [7], multipath formulations through the Green's functions representation [8], full numerical solutions [16] and – most of all – models based on either the Dyadic Green Function (DGF) [17]–[21] or Geometrical optics (Ray Tracing – RT) [2], [5], [14], [15], [22]. DGF is a physics based approach to propagation modelling aiming at the asymptotic evaluation of the overall received field, whereas RT addresses the different field contributions propagating along different optical paths that can be tracked between the transmitting and the receiving locations. Table 1 briefly summarizes the main differences between DGF and RT models.

In this general framework, this paper presents a RT tool specifically conceived for the layered environment, accounting for any type of antenna and for multipath interference, which seems to be especially important when the layers are very thin compared to the communication distance [22]. Compared to standard, general purpose ray tracing models, the layered nature of the propagation environment is here leveraged to come up to a ray tracking process mostly driven by analytical formulations. With respect to [22], where refractions were included to a limited extent, in this paper multiple reflected rays and fourfold transmitted rays are considered and combined to better account for the effect of

cross-layer propagation on the overall received filed strength level. Furthermore, the theoretical soundness of the model is here more comprehensively presented. Finally, some speed up techniques are also discussed and applied to the RT tool to cope with the computational effort to track the huge number of propagation paths resulting from the somehow reverberating nature of the layered scenario. The model reliability is finally checked against measurements carried out at the chip scale as a reference study case. As also stated in Table 1, ray theory is limited to the representation of the radiation field, i.e., it is most of all reliable when far field conditions are satisfied. It is worth pointing out that the far field requirement also concerns the placement of any items and material discontinuities, which should be located in the antenna far field region in order to avoid the possible arising of near field effect that the RT model could not account for. This condition might be not always met in a chip package, where the layers can be very thin and therefore the layers boundaries very close to the on-chip antennas. More in general, in presence of items and material boundaries around the antennas, the theoretical requirement on the clearance of the near-field region imposes a lower bound on the operation frequency, which nevertheless depends case by case on the geometrical layout of the specific application. Shedding some light on the sensitivity of ray simulations accuracy to the compliance with the far field requirement is a further goal of this study.

The proposed RT tool is described in Section II, then Section III highlights some techniques to relieve the computational effort of RT simulations. The measurement campaign performed on fabricated on chip links is described in Section IV, whereas comparisons between measurements and simulations are presented in Section V. Conclusions are finally drawn in Section VI

II. AD HOC RAY TRACING MODEL FOR LAYERED MEDIA

This section is aimed at introducing the RT model for wireless propagation in a layered medium. Description of the environment, of the antenna model and of the procedure for rays computation is addressed in the following sub-sections.

A. DESCRIPTION OF THE SCENARIO

As outlined in Fig. 1, five flat, smooth and infinitely wide layers stacked on top of each other are here considered, made of different lossless materials with refractive index n_{bottom}, n_{down}, n_0, n_{up} and n_{top}, respectively. The three middle layers have finite thickness, namely Δ_{down}, Δ_0 and Δ_{up} in Fig. 1,
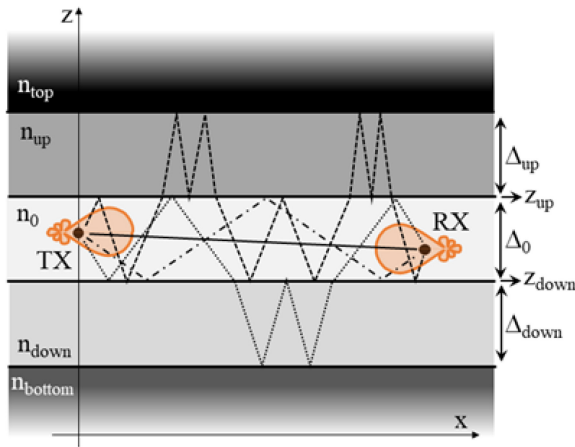
FIGURE 1. Multipath propagation in the layered environment.

and the transmitter (TX) and the receiver (RX) are placed inside the central layer.

B. REPRESENTATION OF THE ANTENNAS

The polarization properties of an antenna placed inside a homogeneous, loss-less medium can be taken into account by its polarization vector:

$$\widehat{p}(\theta, \phi) = \frac{\overrightarrow{E}(r, \theta, \phi)}{\left|\overrightarrow{E}(r, \theta, \phi)\right|} \cdot e^{+j\beta r} \tag{1}$$

where $\overrightarrow{E}(r, \theta, \phi)$ is the far-field radiated in point (r, θ, ϕ) and $\beta = 2\pi/\lambda$ the wave number. Rearranging Eq. (1) leads to the following expression, which highlights three of the major properties of an electromagnetic wave (amplitude, polarization and phase):

$$\overrightarrow{E}(r, \theta, \phi) = \left|\overrightarrow{E}(r, \theta, \phi)\right| \cdot \widehat{p}(\theta, \phi) \cdot e^{-j\beta r} \tag{2}$$

According to the definition of antenna gain function $g(\theta, \phi)$ [23] it holds:

$$\begin{aligned}
\overrightarrow{E}(r, \theta, \phi) &= \sqrt{\frac{\eta \cdot P_a \cdot g(\theta, \phi)}{2\pi}} \cdot \widehat{p}(\theta, \phi) \cdot \frac{e^{-j\beta r}}{r} \\
&= \overrightarrow{E}_0(\theta, \phi) \cdot \frac{e^{-j\beta r}}{r}
\end{aligned} \tag{3}$$

being P_a the antenna absorbed power, η the intrinsic impedance of the medium and $\overrightarrow{E}_0(\theta, \phi)$ the often called "emitted field" (i.e., related to the field value at the conventional distance $r = 1$ m) in the direction of departure (θ, ϕ):

$$\overrightarrow{E}_0(\theta, \phi) = \sqrt{\frac{\eta \cdot P_a \cdot g(\theta, \phi)}{2\pi}} \cdot \widehat{p}(\theta, \phi) \tag{4}$$

Therefore, the spatial radiation properties of a transmitting antenna can be fully described by means of its gain function and its polarization vector.

The same parameters also provide description of the antenna receiving properties, as the power received from an illuminating locally plane wave impinging from the direction of arrival (θ, ϕ) and carrying an incident field $\overrightarrow{E}_{inc}$ can be expressed as [24]:

$$P_{RX} = \frac{\lambda^2}{8\pi\eta} \cdot \left|\sqrt{g(\theta, \phi)} \cdot \widehat{p}(\theta, \phi) \cdot \overrightarrow{E}_{inc}\right|^2. \tag{5}$$

In light of these considerations, the RT tool presented in this work takes into account the antenna properties through a digital description of the functions $g(\theta, \phi)$ and $\widehat{p}(\theta, \phi)$, which are stored into an input file feeding the RT engine. As $\widehat{p}(\theta, \phi)$ is a complex vector, both its θ- and ϕ-complex components must be provided as input information. These data are achieved by means of FDTD simulations of the antenna placed inside a homogeneous medium with refractive index n_0.

C. MATHEMATICAL FRAMEWORK FOR RAY TRACING

Rays propagation inside the scenario sketched in Fig. 1 is ruled by the multipath interference between the direct path and the multiple reflected/refracted paths at the interfaces between the layers. Four types of rays are taken into account by the RT model, as described in the following.

1) DIRECT RAY (D)

This group includes just one ray, directly propagating from the TX to the RX (continuous line in Fig. 1). The corresponding field impinging on the receiving antenna is [2]:

$$\overrightarrow{E}_d = \frac{\overrightarrow{E}_{0d}(\theta_d, \phi_d)}{r_d} \cdot e^{-j\beta_0 r_d} \tag{6}$$

where $\beta_0 = (2\pi/\lambda_0) \cdot n_0$ is the wave number in the antenna layer, r_d the direct path length and $\overrightarrow{E}_{0d}$ the "emitted field" in the direction of the RX. The computation of r_d is straightforward based on the antenna positions as well as $\overrightarrow{E}_{0d}$ can be easily achieved from Eq. (4) by means of the antenna input file and once the Direction of Departure (DoD) of the ray (θ_d, ϕ_d) has been estimated. The ray Direction of Arrival (DoA) (θ_a, ϕ_a) at the receiver can be also computed from the antenna positions.

2) MULTIPLE REFLECTED RAYS (RM)

This class encompasses all the rays undergoing reflections at the upper and lower boundary of the antenna layer (dashed-dotted line in Fig. 1). The field carried to the RX by a m-reflected ray can be expressed as [2]:

$$\overrightarrow{E}_m = \frac{\overrightarrow{E}_{0m}(\theta_m, \phi_m)}{r_m} \cdot e^{-j\beta_0 r_m} \cdot \Pi_m, \quad m \geq 1 \tag{7}$$

being r_m the traveled distance, $\overrightarrow{E}_{0m}(\theta_m, \phi_m)$ the emitted field in the DoD of the ray and Π_m the product of the m Fresnel reflection coefficients. According to the image principle, r_m can be computed as the straight distance between the RX and a "m_{th} virtual transmitter" (V_{TX} in Fig. 2) that
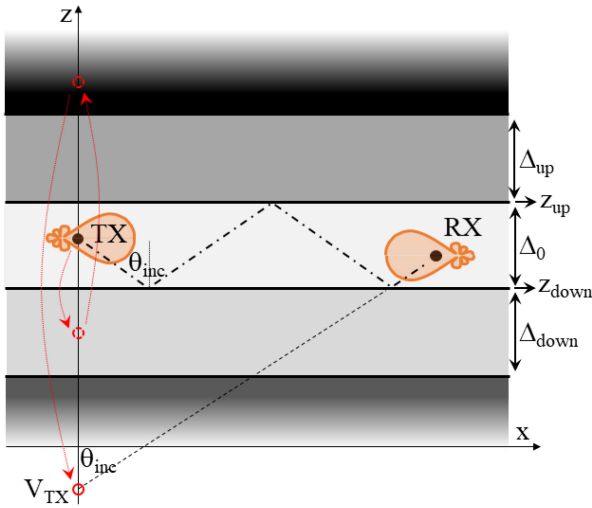
FIGURE 2. Rays reflected in the antenna layer.

is the "mirror image" of the TX (if $m = 1$) or of the $(m-1)_{th}$ V_{TX} (otherwise) with respect to the reflecting plane.

Closed-form, analytical expressions for the position of the m_{th}-order V_{TX} are reported in [2]. Once the virtual transmitter is known, the ray length r_m, the incidence angle θ_{inc} and the DoD/DoA of the ray can be easily computed, and therefore the value of $\overrightarrow{E}_{0m}$ and Π_m. It is worth pointing out that the same number of reflections m always corresponds to two different rays, the former with the first reflection on the upper interface, the latter on the lower one. The class cardinality is therefore:

$$N_{Rm} = 2, \quad \forall\, m \geq 1. \tag{8}$$

### 3) MULTIPLE REFLECTED, TWOFOLD TRANSMITTED RAYS (RMT2)

Thanks to the double transmission, these rays exit the antenna layer and propagate inside either the upper or the lower layer before falling back to the RX (dotted line in Fig. 1). The V_{TX} expedient can be still relied on to account for the multiple reflections occurring in the central layer before the first refraction. Similarly, a "virtual receiver" (V_{RX} in Fig. 3) can be also introduced to replace the multiple reflections in the antenna layer after the second refraction.

If k reflections take place in the upper/lower layer, rays refracting through the lower and the upper interface comply with the following Eqs. (9) and (10), respectively [22] (further details also in Appendix A):

$$(z_{VTX} - z_{down}) \cdot \tan(\theta_{inc}) + (k + 1) \cdot \Delta_{down} \cdot \tan(\theta_t) +$$
$$+ (z_{VRX} - z_{down}) \cdot \tan(\theta_{inc}) = x_{RX} - x_{TX} \tag{9}$$
$$(z_{up} - z_{VTX}) \cdot \tan(\theta_{inc}) + (k + 1) \cdot \Delta_{up} \cdot \tan(\theta_t) +$$
$$+ (z_{up} - z_{VRX}) \cdot \tan(\theta_{inc}) = x_{RX} - x_{TX} \tag{10}$$

being θ_i, θ_t the incidence and refraction angles, z_{VTX}, z_{VRX} the z-coordinates of the V_{TX}/V_{RX}, z_{up}, z_{down} the position of the upper and of the lower interface, and x_{TX}, x_{RX} the x-coordinates of the TX and of the RX, respectively (Fig. 3).
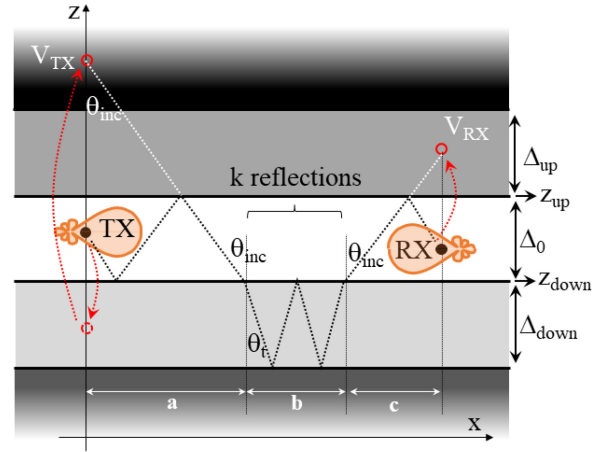
FIGURE 3. Twofold refracted rays.

As θ_t depends on θ_i through the Snell's law, and z_{VTX}, z_{VRX} can be expressed by means of the formulas discussed in [2], θ_i can be quickly estimated from (9) and (10) and therefore the refraction angle θ_t, the ray DoD/DoA as well as the travelled distance in the different layers can be also computed. Finally, the wave field reaching the RX through m total reflections and two refractions can be expressed as [22]:

$$\overrightarrow{E}_{m2,i} = \overrightarrow{E}_{0m2,i}(\theta_{m2,i}, \phi_{m2,i}) \cdot \frac{e^{-j\beta_0 r_{0,i}} \cdot e^{-j\beta_{up/down} r_{up/down,i}}}{r_{0,i} + r_{up/down,i}}$$
$$\times\ \Pi_{m,i} \cdot T_{2,i} \tag{11}$$

being $\beta_{up/down} = (2\pi/\lambda_0) \cdot n_{up/down}$ the wave number in the upper/lower layer, $r_{0,i}$ and $r_{up/down,i}$ the path length travelled inside the antenna layer and the upper/lower layer, respectively, $T_{2,i}$ the product of the two refraction coefficients (into and from the upper/lower layer), $\Pi_{m,i}$ the product of the m reflection coefficients, and $\mathbf{E}_{0m2,i}$ the emitted field in the DoD $(\theta_{m2,i}, \phi_{m2,i})$ of the ray. As a multitude of different rays experiencing m reflections and two refractions is present, the sub-script i in (11) stands for the i_{th} ray belonging to the class RmT2. As proved in Appendix B, the overall number of rays inside the class RmT2 is:

$$N_{RmT2} = 2 \cdot \sum_{k=1,\,k\,odd}^{m} (m - k + 1), \quad \forall\, m \geq 1. \tag{12}$$

4) MULTIPLE REFLECTED, FOURFOLD TRANSMITTED RAYS (RMT4)

This cluster corresponds to the rays experiencing four transmissions, i.e., penetrating the upper or the lower layer twice (dashed line in Fig. 1), or both the layers once. With reference to Fig. 4, the following characteristic equation holds for each ray with the four refractions across the upper interface (Appendix A):

$$\tan(\theta_{inc}) \cdot \left[|z_{up} - z_{VTX}| + |z_{up} - z_{VRX}| + (k_3 + 1) \cdot \Delta_0\right]$$
$$+\ \tan(\theta_t) \cdot (k_1 + k_2 + 2) \cdot \Delta_{up} = x_{RX} - x_{TX} \tag{13}$$

where k_1 / k_2 / k_3 represents the number of reflections occurring between the first and the second / the third and
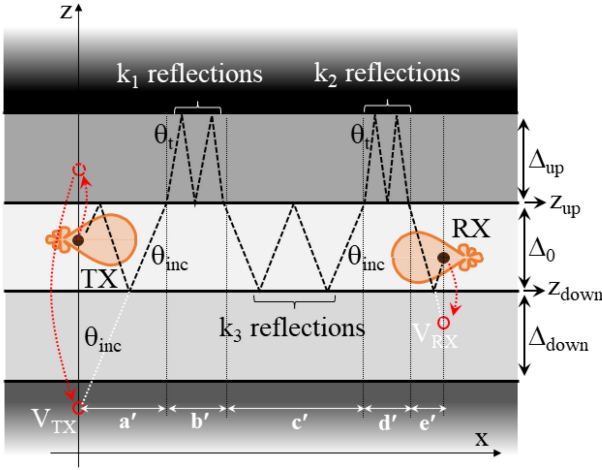
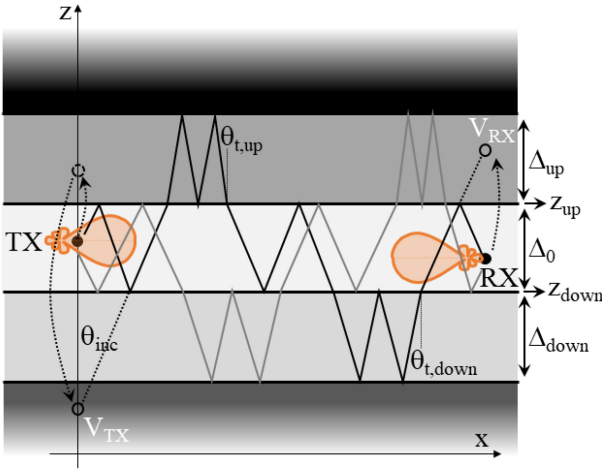**FIGURE 4.** Double refraction in the same layer.

FIGURE 5. Double refraction in different layers.

the fourth / the second and the third refraction, respectively (Fig. 4). Similarly, rays refracting four times through the lower interface comply with the following equation:

$$\tan(\theta_{inc}) \cdot \left[\left| z_{down} - z_{V_{TX}} \right| + \left| z_{down} - z_{V_{RX}} \right| + (k_3 + 1) \cdot \Delta_0 \right]$$
$$+ \tan(\theta_t) \cdot (k_1 + k_2 + 2) \cdot \Delta_{down} = x_{RX} - x_{TX} \quad (14)$$

With reference to the rays crossing both the upper and the lower interface (Fig. 5), different characteristic formulas are achieved, depending on whether the ray firstly penetrates the upper layer (black line in Fig. 5) or the lower one (grey line in Fig. 5). Equation (15) corresponds to the former case, whereas Eq. (16) holds for the latter. Of course, $\theta_{t,up}$ and $\theta_{t,down}$ represent the refraction angles in the upper and in the lower medium, respectively (Fig. 5).

$$\tan(\theta_{inc}) \cdot \left[\left| z_{up} - z_{V_{TX}} \right| + \left| z_{down} - z_{V_{RX}} \right| + (k_3 + 1) \cdot \Delta_0 \right]$$
$$+ (k_1 + 1) \cdot \Delta_{up} \cdot \tan(\theta_{t,up})$$
$$+ (k_2 + 1) \cdot \Delta_{down} \cdot \tan(\theta_{t,down}) = x_{RX} - x_{TX} \quad (15)$$
$$\tan(\theta_{inc}) \cdot \left[\left| z_{down} - z_{V_{TX}} \right| + \left| z_{up} - z_{V_{RX}} \right| + (k_3 + 1) \cdot \Delta_0 \right]$$
$$+ (k_2 + 1) \cdot \Delta_{up} \cdot \tan(\theta_{t,up})$$
$$+ (k_1 + 1) \cdot \Delta_{down} \cdot \tan(\theta_{t,down}) = x_{RX} - x_{TX} \quad (16)$$

As already discussed for the twofold refracted rays, θ_{inc} can be computed from Eqs. (13)-(16). The refraction angle(s), the DoD/DoA of the ray and its length in the different layers can be also computed afterwards. The field conveyed to the RX by the i_{th} ray undergoing m total reflections and four transmissions can be finally computed as:

$$\vec{E}_{m4,i} = \vec{E}_{0m4,i}\left(\theta_{m4,i}, \phi_{m4,i}\right)$$
$$\times \frac{e^{-j\beta_0 r_{0,i}} \cdot e^{-j\beta_{up} r_{up,i}} \cdot e^{-j\beta_{down} r_{down,i}}}{r_{0,i} + r_{up,i} + r_{down,i}} \cdot \Pi_{m,i} \cdot T_{4,i}$$

(17)

being $r_{up,i}$ and $r_{down,i}$ the total travelled distance in the upper and in the lower layers, and $T_{4,i}$ the product of the four refraction coefficients.

The cardinality of the class RmT4 is (Appendix B):

$$N_{RmT4} = N_{RmT4}^{UP} + N_{RmT4}^{DOWN} + N_{RmT4}^{UP-DOWN} + N_{RmT4}^{DOWN-UP}$$

(18)

$$N_{RmT4}^{UP} = \begin{cases} \sum_{k_1=1,odd}^{m-2} \sum_{k_2=1,odd}^{m-k_1-1} \sum_{k_3=1,odd}^{m-k_1-k_2} m \\ \quad - (k_1 + k_2 + k_3) + 1 \quad \forall\, m \geq 3 \\ 0 \quad \text{otherwise} \end{cases}$$

$$N_{RmT4}^{DOWN} = N_{RmT4}^{UP}$$

(19)

$$N_{RmT4}^{UP-DOWN} = \begin{cases} \sum_{k_1=1,odd}^{m-1} \sum_{k_2=1,odd}^{m-k_1-1} \sum_{k_3=0,even}^{m-k_1-k_2} m \\ \quad - (k_1 + k_2 + k_3) + 1 \quad \forall\, m \geq 2 \\ 0 \quad \text{otherwise} \end{cases}$$

$$N_{RmT4}^{DOWN-UP} = N_{RmT4}^{UP-DOWN}$$

(20)

It is worth pointing out that the reliability of the RT approach is commonly limited to the presence of low-loss materials, since the power decay with distance in Eqs. (6), (7), (11) and (17) clearly corresponds to the propagation of uniform waves in lossless media.

After the N_r rays belonging to the different classes have been computed (up to a maximum reflection order m_{max}), the overall received power is the result of the interference among them, i.e., [24]:

$$P_{RX} = \frac{\lambda^2}{8\pi\eta} \cdot \left| \sum_{i=1}^{N_r} \sqrt{g_{RX}(\theta_{a,i}, \phi_{a,i})} \cdot \hat{p}_{RX}(\theta_{a,i}, \phi_{a,i}) \cdot \vec{E}_{inc,i} \right|^2$$

(21)

being $\mathbf{E}_{inc,i}$ the impinging field carried by the i_{th} ray arriving from the direction $(\theta_{a,i}, \phi_{a,i})$.

It can be finally noted that N_r quickly increases as the reflection order is raised up. The number of rays to be tracked for each TX, RX pair is reported in Table 2 for some values of m_{max}. As already pointed out in the Introduction and further discussed in Section V, a layered wireless channel can be quite a reverberating propagation environment, and therefore simulation accuracy cannot be achieved unless a large number of reflections is considered. In case many TX/RX locations have to be taken into account, e.g., to investigate fast fading statistics, the overall number of rays to be traced can easily rise up to several millions. Since general purpose

TABLE 2. Rays number per (TX, RX) pair and for different reflection order.

		Rays Number
Reflection order (m_{max})	5	111
	10	1'237
	30	143'709
	50	1'601'181
	100	46'133'611

TABLE 3. Percentage rays reduction for different reflection order.

		Speed-up Technique	
		Correction Factors	Enhanced Model
Reflection order (m_{max})	5	34%	90%
	10	76%	98%
	30	98%	99.9%
	50	99.5%	99.9%
	100	99.9%	99.9%

RT tools might hardly endure the corresponding computational effort, the *ad hoc* RT model described in this section has been developed. Nevertheless, it can also require long simulation time in the utmost challenging situations (e.g., on-chip wireless communications at optical frequencies), to the extent that it is worth investigating some solutions to reduce the ray simulation burden. This issue is addressed in the following section.

III. SPEED-UP TECHNIQUES

Two different solutions are considered to reduce the number of rays traced within each RT simulation run, referred to as "Correction Factor model" and "Enhanced model" in the following sub-sections. Both the approaches achieve great computational gain at the expense of the theoretical soundness, to an extent that will be better investigated in Section V.

A. CORRECTION FACTOR MODEL

The rays number reduction is applied to the classes RmT2 and RmT4, which are the largest. In the former case, ray tracing is limited to the paths with just one reflection on the top or on the bottom interface, i.e., with k = 1 in Fig. 3. As explained in Appendix B (Eq. (B1)), the number of rays refracting across the upper or the lower interface drops to:

$$P(m, 1) = \frac{m!}{(m-1)!} = m \qquad (22)$$

In order to approximately compensate for the reduced number of rays, the amplitude of each ray undergoing m overall reflections is increased by the following correction factor:

$$CF_{RmT2}(m) = \sqrt{\frac{N_{RmT2}^{UP}}{P(m, 1)}} = \sqrt{\frac{N_{RmT2}^{DOWN}}{P(m, 1)}} \qquad (23)$$

where the expression for N_{RmT2}^{UP}, N_{RmT2}^{DOWN} are provided by Eq. (B3). In practice, the intensity of each ray is increased by the ratio between the overall number of existing rays and the number of rays actually tracked.

The same procedure is then easily extended to the class RmT4. With reference to the rays refracting across the same interface (either upper or lower), ray tracing is limited to the paths having $k_1 = k_2 = k_3 = 1$ (Fig. 4), corresponding to a number of rays equal to (Appendix B, Eq. (B4)):

$$P(m, 1, 1, 1) = \frac{(m-2)!}{(m-3)!} = m - 2, \quad m \geq 3 \qquad (24)$$

The following correction factors are then applied:

$$CF_{RmT4}(m) = \sqrt{\frac{N_{RmT4}^{UP}}{P(m, 1, 1, 1)}} = \sqrt{\frac{N_{RmT4}^{DOWN}}{P(m, 1, 1, 1)}} \qquad (25)$$

being N_{RmT4}^{UP}, N_{RmT4}^{DOWN} expressed by Eq. (B5). As far as the rays refracting into both the upper and the lower layer are concerned (Fig. 5), the analysis is instead limited to $k_1 = k_2 = 1$, $k_3 = 0$. The number of rays actually traced and the corresponding correction factors are expressed by the following equations, respectively:

$$P(m, 1, 1, 0) = \frac{(m-1)!}{(m-2)!} = m - 1, \quad m \geq 2 \qquad (26)$$

$$CF'_{RmT4}(m) = \sqrt{\frac{N_{RmT4}^{UP-DOWN}}{P(m, 1, 1, 0)}} = \sqrt{\frac{N_{RmT4}^{DOWN-UP}}{P(m, 1, 1, 0)}} \qquad (27)$$

where $N_{RmT4}^{UP-DOWN}$, $N_{RmT4}^{DOWN-UP}$ are reported in Eq. (B6).

The percentage reduction in the number of rays with respect to the full ray approach is shown in Table 3 for some different reflection order m_{max}. Of course, a proportional reduction in the simulation time must be also expected.

B. ENHANCED MODEL

In this case, the computational gain relies on [25], where some "enhanced" coefficients are proposed to model wave reflection from/transmission through a plane, smooth layer of finite thickness. Such coefficients consist of closed form, analytical expressions accounting for the multiple bounces experienced by the signal propagating between the layer boundaries (Fig. 6).

Although the formulas reported in [25] assume the layer surrounded by the same material, they have been here extended to the case where different materials are instead present at the different sides of the slab ($\varepsilon_1 \neq \varepsilon_3$ in Fig. 6). As proved in Appendix C, the enhanced reflection coefficient is:

$$R_{en} = R_{12} + \frac{T_{12} \cdot T_{21}}{R_{12}} \cdot \frac{R_{23} \cdot R_{12} \cdot P_d^2 \cdot P_a}{1 + R_{23} \cdot R_{12} \cdot P_d^2 \cdot P_a} \qquad (28)$$

being all the symbols defined in the Appendix.

The strategy applied by the enhanced propagation model is then quite straightforward, as it only tracks the direct path and the rays reflected inside the antenna layer, but applying at each reflection point the enhanced reflection coefficient rather than the simpler Fresnel one. In other words, multiple
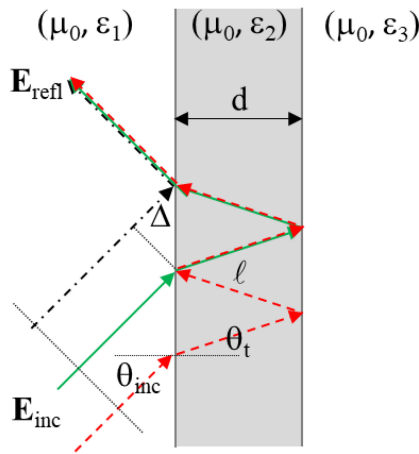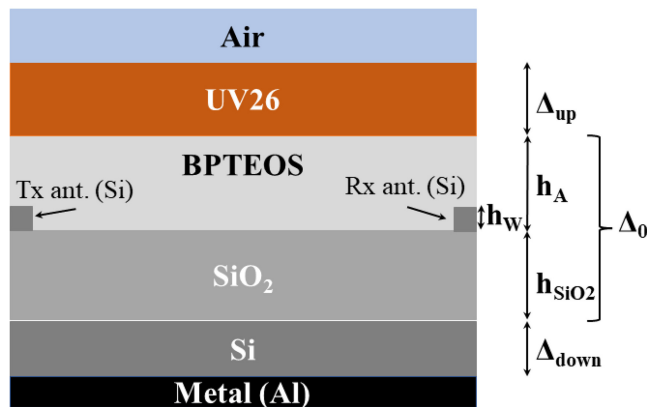
FIGURE 6. Ray description of reflection from a slab.

FIGURE 7. Layered structure of the fabricated wireless links.

TABLE 4. Layer parameters.

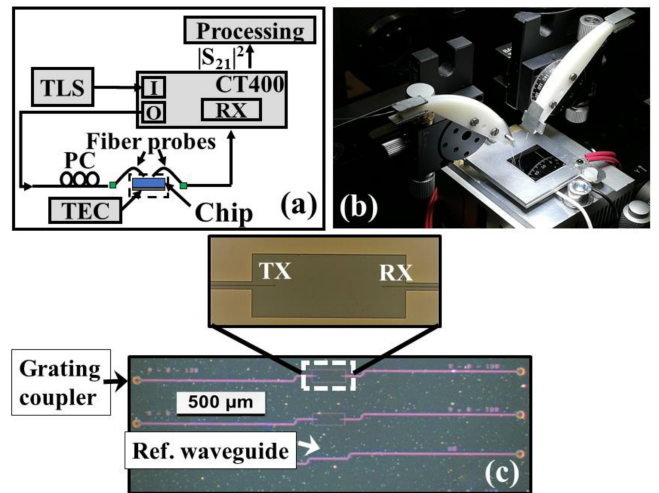| Layer	Material	Refractive index	Thickness
Lower	Si	$n_{down} = 3.476$	$\Delta_{down} = 675 \mu m$
Substrate	SiO$_2$	$n_{SiO2} = 1.445$	$h_{SiO2} = 3 \mu m$
Antenna - layer - waveguide	 BPTEOS Si	 $n_A = 1.453$ $n_W = 3.476$	 $h_A = 0.3 \mu m$ $h_W = 0.22 \mu m$
Upper	UV26	$n_{up} = 1.526$	$\Delta_{up} = 3.78 \mu m$

FIGURE 8. Block scheme of the measurement equipment (a), microscope image of the fabricated links on-chip (b) and measurement set-up (c).

reflections inside the upper and the lower layer are somehow "embedded" onto the rays reflected in the antenna layer by means of the enhanced reflection coefficients. The corresponding percentage reduction in the number of considered rays is also included in Table 3. As clearly stated in [25] from the title, the enhanced coefficient should be applied to reflection from thin layers, as it may turn out to be rather inaccurate otherwise.

IV. ON-CHIP PATH-GAIN MEASUREMENTS

A measurement campaign has been carried out on real wireless links, fabricated in standard SOI technology and designed to operate in the optical C-band (1530 nm÷1565 nm). The layered structure of the chip (Fig. 7) consists of a lower bulk of Silicon ($\Delta_{down} = 675 \mu m$) coated with a layer of SiO$_2$ ($h_{SiO2} = 3 \mu m$) further overlayed by a thin film of Silicon ($h_W = 220 \, nm$), where standard Si waveguides and the antennas are etched. Waveguides and antennas are then covered by a thin layer ($h_A = 300 \, nm$) of borophosphorous tetraethyl orthosilicate (BPTEOS), being easily planarized and showing a refractive index very close to Silica (Table 3) [26]. Finally,

a polymer-based top layer made of UV26 ($\Delta_{up} = 3.78 \mu m$) has been deposited above the BPTEOS.

As the investigation is mainly oriented to propagation modeling, the antennas have been designed by simply tapering the silicon waveguides according to what discussed in [27]. According to the scheme in Fig. 7, the transmitting and the receiving antennas are placed at the same level within the chip, always facing each other. A specific link is fabricated for each different link distance.

Thickness and refractive index of the different materials are summarized in Table 4. Propagation losses in silicon and silicon dioxide are respectively equal to nearly 0.026 dB/cm [28] and 0.3 dB/km [29], and therefore are fully negligible at chip scale. BPTEOS is also commonly considered as a lossless material.

The layer thickness and the materials considered in Fig. 7 and Table 4 are compliant with the chip package structure considered in some previous works [5], [7].

Measurements aimed at the assessment of the received to transmitted power ratio, referred to as Path Gain (PG) in the following.

The test bench utilized is shown in Fig. 8(a) and Fig. 8(b). It consists of a tuneable laser source (TLS) TUNICS T-100S-HP and a passive optical component tester (CT400) which

were used to measure the $|S_{21}|^2$ for each device under test. A picture of the fabricated on-chip optical wireless links and exciting waveguide structure is shown in detail in Fig. 8(c).

Fiber probes are coupled with the chip through taper gratings fabricated at the input/output sections of the waveguides exciting the antennas of the wireless links, to allow for signal coupling from the top side (Fig. 8(b)). The coupling was maximized thanks to micro positioners and a polarization controller (PC). Furthermore, silicon reference waveguides were also fabricated on the same chip, to take into account possible signal losses not strictly arising from the propagation channel. In the end, PG values have been computed as:

$$PG_{dB} = 20 \cdot \log_{10}|S_{21}|_{\text{device under test}}$$
$$- 20 \cdot \log_{10}|S_{21}|_{\text{ref. waveguide}} \quad (29)$$

During measurements, the chip was laid on a flat support made of aluminum, which acted as bottom layer and is therefore included in Fig. 7.

Possible environment perturbations are also minimized through the use of a Thermo-Electric Controller (TEC).

Further details on the design of the optical wireless links and of the measurement equipment can be found in [22] and [26].

V. RESULTS AND DISCUSSION

The prediction accuracy of the RT models presented in Sections II and III has been checked against PG measurements carried out at chip level by means of the measurement procedure outlined in Section IV [26]. Ray simulations have been run in the layered scenario outlined in Fig. 7 and Table 4, for link distance ranging from 20 μm to 1500 μm with 1 μm step. As BPTEOS has a refractive index very close to SiO2, a single silica layer with thickness $\Delta_0 = h_{SiO2} + h_A = 3.3$ μm has been considered in the RT simulations, for the sake of simplicity. FDTD analysis has been relied on to feed the RT engine with an input file storing the θ- and the φ-complex components of the tapered antennas far-field. The propagation frequency is $f_0 \approx 193.55$ THz, corresponding to $\lambda_0 = 1.55$ μm. A suitable reflection order m_{max} needs to be identified beforehand, as the simulation accuracy is clearly poor if m_{max} is too low, whereas the computation time becomes extremely long if it is too large. To such aim, the root mean square difference (RMSD) between PG assessments achieved with reflection order equal to m_{max} and $(m_{max} + 5)$ is plotted in Fig. 9 for increasing values of m_{max}.

Not surprisingly, the number of required reflections to be considered increases with the communication distance. In fact, every ray inside the layered environment gets closer to grazing incidence at longer distance – especially when the communication range greatly exceeds the layers thickness - and therefore keeps a large intensity despite the number of undergone interactions and the length of the travelled path. According to Fig. 9, about 60/70 reflections are necessary to
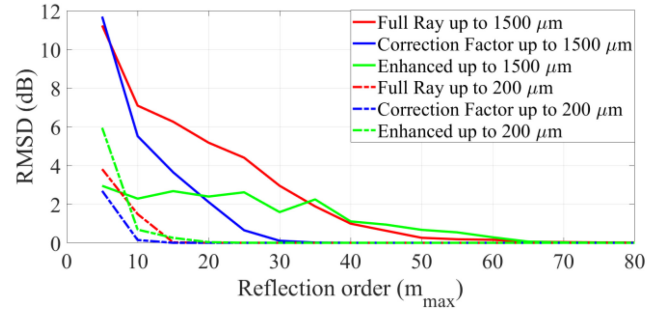

FIGURE 9. Root mean square difference between the outcomes of ray simulations for different reflection order.
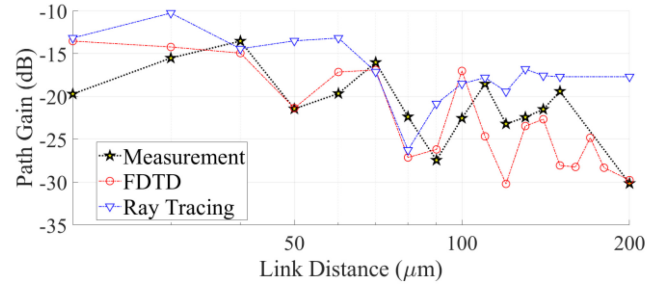

FIGURE 10. FDTD and RT simulations vs. on-chip measurements.

model propagation up to 1500 μm, whereas 15/20 reflections would be enough reducing the maximum link distance to 200 μm. Results shown in the following refer to a reflection order $m_{max} = 70$.

In order to investigate possible impairment on the RT reliability due to the presence of materials interfaces in the near field region (UV26 and Silicon are placed respectively at 0.3 μm and 3 μm from the antennas), PG has been computed by means of FDTD and RT and is checked against measurement in Fig. 10. Of course, the FDTD method can account for both near- and far-field interactions, whereas only the latter can be tracked by the RT tool. The comparison is limited to the range [20μm ÷ 200μm] because of the computational load required by FDTD. Although FDTD results look better overall, RT can also track the spatial trend fairly well. Therefore, the accuracy of RT does not seem heavily affected by possible near field effects, at least in the case under test. This is also intuitively justified by the small refractive index contrast between the layer materials.

Simulated PG values corresponding to different RT simulation runs are then reported in Fig. 11, together with measurement over the full range [20μm ÷ 1500μm]. As the silicon layer is much thicker than the wavelength ($\Delta_{down} = 675$ μm and $\lambda = 1.5$ μm), the modified reflection coefficients introduced by the enhanced model have been applied to reflections at the upper UV26 layer only.

The prediction accuracy of the ray approach is summed up in Table 5 in terms of RMSE, mean error ed error std. deviation between simulations and measurement. The run time is also reported for each case, and refers to a commercial
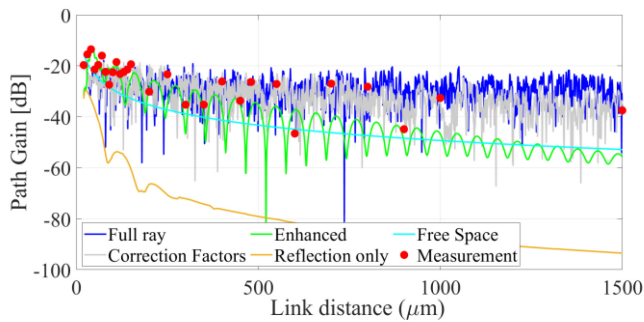
FIGURE 11. Point specific comparison between measurements and simulations.

FIGURE 12. Comparison between spatially averaged measurements and simulations.

TABLE 5. Accuracy of the different models.

	Mean Err. (dB)	σ_{err}(dB)	RMSE (dB)	Run Time
Full ray	-2.9	9	9.4	98 h
Correction Factor	-3.5	7.2	7.9	614 s
Enhanced Reflection	-6	7.8	9.8	3 s
Reflection only	-37.4	13.1	39.6	2 s

TABLE 6. Models accuracy after spatial average.

	Mean Err. (dB)	σ_{err}(dB)	RMSE (dB)
Full ray	-2.9	3.4	4.4
Correction Factor	-3.3	3.1	4.5
Enhanced Reflection	-3.3	2.8	4.3

workstation equipped with an Intel Xeon CPU E5 2620V4 @ 2.1 GHz.

As already pointed out in [22], refraction plays a crucial role, as simulations limited to reflections only are fully unreliable. Since the silica layer has a refractive index lower than UV26 and silicon (Table 4), rays reflecting inside the antenna layer always experience some power leakage at the bounding interfaces. Conversely, waves refracting into the UV26 or the Silicon layers can benefit from the total reflection occurring at both the UV26/Air boundary (at least for incidence greater than the critical angle $\theta_c \approx 41°$) and the silicon/metal interface. Therefore, part of the energy outgoing the antenna layer is then brought back by the total reflection at the outer interfaces.

Extending the RT simulations to refraction greatly reduces the RMSE values, which nevertheless keep approximately larger than 8 dB in Table 5. This is explained by the many factors limiting reliable fast fading tracking through RT [24]. Although the on-chip propagation channel appears simpler than other scenarios in terms of environmental cluttering, unavoidable imprecisions in the descriptions of either the layers thickness/materials or the antennas radiation properties can dramatically affect the phase relations between the received rays compared to the actually received multipath contributions.

Fast fading has been then removed by averaging both simulated and measured PG values over a spatial interval of 100 μm. The corresponding average signal strength range dependence is reported in Fig. 12, where some large scale fluctuations still affect both measurements and RT predictions. As also highlighted in Table 6, the measurement – simulation comparison is now much more fair, with RMSE dropped to about 4.5 dB for all the ray approaches somehow
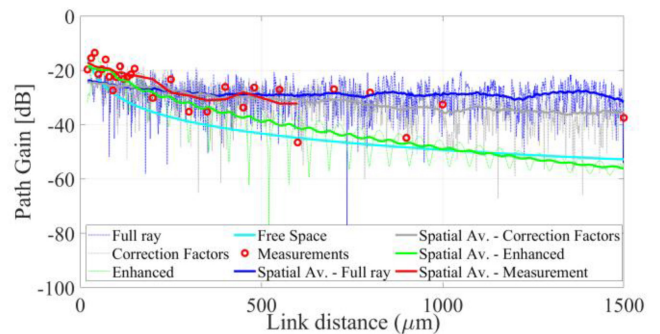
accounting for refraction. Although large scale fading is generally related to shadowing from obstacles, it is instead still caused by multipath effects in layered propagation structures. Therefore, the disagreement between measured and simulated data in Fig. 12 and Table 6 is also due to some imprecisions in the description of either the layers thickness/materials or the antenna properties, which finally lead to inaccuracies in the evaluation of the rays amplitude/phase relations.

Anyway, the achieved performance after fast fading removal is in general agreement with previous studies, where RMSE values between 7 and 10 dB [24] and up to 5 dB [29] are for instance reported for the urban and the tunnel environment, respectively.

Although the "Enhanced RT model" is by far less reliable than the full ray and the correction factors models at the larger range (Fig. 11 and Fig. 12), it basically shares the same RMSE in Table 6. This is basically due to the non-uniform distribution of measurements over the 20μm ÷ 1500μm range. In order to increase the spatial density of the optical circuits manufactured onto the silicon wafer, 14 out of 28 samples correspond to link distance lower than 150 μm – where the enhanced model performs quite well -, whereas just 7 antenna pairs were placed at a distance longer than 500 μm. Of course, the 14 samples at the shorter distance affect the computation of the RMSE more than the 7 furthest, simply because they are more.

Conversely, both the "Full ray" approach and the introduction of the correction factors clearly provide better accuracy at the longer distance, where RT can be mostly important as numerical methods like FDTD, MoM, etc. cannot represent viable solutions because of their heavy computational burden.
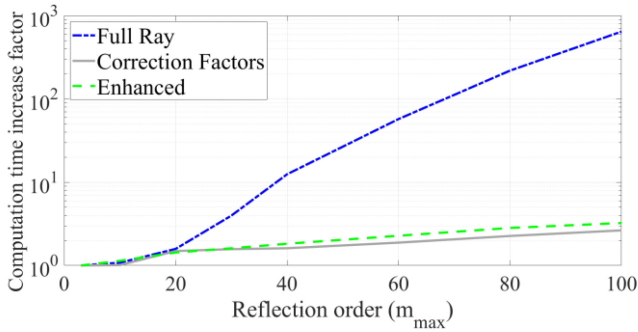
FIGURE 13. Computation time increase factor for increasing reflection order.
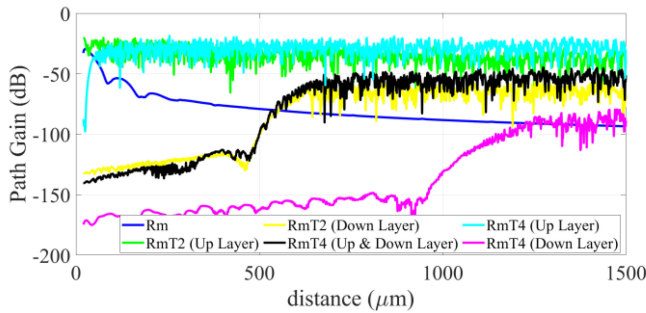

FIGURE 14. Contribution of the different rays classes to the total signal intensity.

Since the speed-up techniques described in Section III greatly reduce the number of tracked rays (Table 3), the simulation time in Table 5 also decreases accordingly. The full ray approach and the speed up techniques are also compared in Fig. 13 in terms of computational cost for increasing reflection order. In order to get rid of the hardware settings, the normalized run time (computation increase factor) is reported in Fig. 13. The speed up solutions can clearly keep the simulation time quite short regardless of the reflection order.

It is also worth mentioning that the number of rays traced by the full ray model amounts to more than 12 billion in the considered scenario, i.e., a number that general purpose ray tracing tools for propagation prediction might hardly afford, unless the latest implementation on GPU cards are envisaged [31]. On the other hand, the full ray model is likely to be necessary to extend the investigation to wideband analysis, i.e., to temporal dispersion/frequency selectivity, although this goes beyond the scope of this manuscript.

Moreover, the full ray approach can also provide insight into how the different rays (sub-)classes contribute to the total signal strength. This is reported in Fig. 14, where the different PG curves have been achieved enabling the different rays classes in turn. As already discussed, reflections only (Rm class, blue line in Fig. 14) do not convey the greatest power, at least in the case under test. Conversely, rays experiencing two or four refractions across the silica/UV26 upper boundary (green and cyan lines in Fig. 14) turn out to be the most powerful contributions. As the antenna and the upper layer basically have the same thickness and quite similar

refractive index (Table 4), rays restricted to the silica layer only have lengths and incidence angles similar to the rays also flooding the UV26 layer (for the same number of reflections, of course). Nevertheless, the silica and the UV26 layers altogether represent a more reverberating duct compared to the silica layer alone, because of the already discussed possible occurrence of total reflection, and this can explain the different results in Fig. 14.

PG related to the rays refracting into the lower silicon layer is instead the result of different, contrasting effects (black, yellow and magenta curves in Fig. 14). On the one hand, they again benefit from the total reflection effect occurring the lowest metal interface; on the other hand, they have to cross the silicon slab, that is much thicker than the other layers. This leads to much longer travelled lengths compared to rays just reflecting inside the antenna layer – for the same number of overall reflections – and to smaller incidence angles, i.e., to directions of departure/arrival out of the main radiation lobe of the antennas, unless they are well far apart. Overall, refraction into the lower layer results quite negligible for the shorter distance and corresponds to PG values always and at least 10/15dB lower compared to the intensity carrier by the up-refracted rays.

The simulation accuracy of the full ray model can be then traded off against the computation time by limiting the simulation to the actually powerful classes of rays. For instance, cutting out the rays refracting into the lower layer reduces the simulation time from 98 h to nearly 23 h (this is, a reduction of 76.5%) for basically the same accuracy (RMSE = 4.46dB after spatial average).

Clearly, the relative weight of the different rays classes is strongly dependent on the properties of the layered scenario, i.e., to the layers thickness and filling materials, as well as on the antenna radiation properties and positions. Anyway, the ray approach can be more easily tailored to the specific case, whereas different numerical methods (e.g., DGF, FDTD, etc.) look much less flexible.

VI. CONCLUSION
A ray tracing based algorithm specifically conceived for electromagnetic propagation modeling in layered scenarios has been presented in this study. As the layered propagation channel often displays a somehow reverberating nature, rays tracking is mainly carried out through analytical formulations, thus limiting the corresponding computation effort compared to general purpose ray-based algorithms and other numerical methods. Some speed up techniques have been also discussed in the paper in order to further reduce the computational burden.

The proposed model can complement traditional approaches (like the Dyadic Green Function method) for the description of propagation in layered media, e.g., when antennas different from simple current elements must be considered, when propagation at (very) far distance (with respect to the wavelength) is concerned, or the dispersive properties of the wireless channels have to be investigated.

The model accuracy is assessed through comparison with measurements carried out at chip-scale in the C optical band as a reference study case. Although on-chip wireless channels might not always satisfy the conditions required by the ray tracing theory (e.g., about far-field conditions or material losses), an RMSE equal to about 4.5 dB has been achieved for path gain prediction, that is in agreement with previous, general assessment of ray tracing accuracy. Computation time ranges from few seconds to tens of hours depending on the case. It is worth noting that more than 12 billion rays must be traced in the considered scenario, and therefore even the slowest, full ray model turns out to be much quicker compared to numerical methods like FDTD or general purpose ray models. In light of its flexibility, the model can also provide physical insight into the contribution of the different classes of rays to wireless communications, which can be helpful to tailor the antennas and other link parameters to the specific properties of the wireless channel.

Follow up activities will be the ray-based investigation of the wideband properties of the layered propagation channel. Open challenges concern the extension of the ray approach to the presence of obstacles in the antenna layer (e.g., crossing fibers or cables, in the chip scale reference case), or the management of not negligible material losses that may rise up at some frequencies. More in general, propagation in layered media takes its place at the borderline between different modeling approaches, spanning numerical methods, ray based algorithms and integral solutions, among others. A comprehensive comparison of the possible methodologies and their accuracy and convenience for different applications is also worth following investigations.

APPENDIX A

With reference to the twofold refracted rays, the following geometrical relation can be easily established (Fig. 3):

$$a + b + c = x_{RX} - x_{TX} \tag{A1}$$

The length of segments a, b and c can be then expressed as follows:

$$a = |z_{VTX} - z_{down}| \cdot \tan(\theta_{inc}) \tag{A2}$$

$$b = (k + 1) \cdot \Delta_{down} \cdot \tan(\theta_t) \tag{A3}$$

$$c = |z_{VRX} - z_{down}| \cdot \tan(\theta_{inc}) \tag{A4}$$

Introducing Eqs. (A2)-(A4) into (A1) leads to:

$$|z_{VTX} - z_{down}| \cdot \tan(\theta_{inc}) + (k + 1) \cdot \Delta_{down} \cdot \tan(\theta_t) +$$
$$+ |z_{VRX} - z_{down}| \cdot \tan(\theta_{inc}) = x_{RX} - x_{TX} \tag{A5}$$

that exactly corresponds to eq. (9). Eq. (10) can be proved in a similar way.

As for the fourfold refracted rays, the following starting relationship can be determined from Fig. 4:

$$a' + b' + c' + d' + e' = x_{RX} - x_{TX} \tag{A6}$$

where:

$$a' = |z_{VTX} - z_{up}| \cdot \tan(\theta_{inc}) \tag{A7}$$

$$b' = (k_1 + 1) \cdot \Delta_{up} \cdot \tan(\theta_t) \tag{A8}$$

$$c' = (k_3 + 1) \cdot \Delta_0 \cdot \tan(\theta_{inc}) \tag{A9}$$

$$d' = (k_2 + 1) \cdot \Delta_{up} \cdot \tan(\theta_t) \tag{A10}$$

$$e' = |z_{RX} - z_{up}| \cdot \tan(\theta_{inc}) \tag{A11}$$

Then, by means of simple substitutions:

$$\tan(\theta_{inc}) \cdot \left[|z_{up} - z_{VTX}| + |z_{up} - z_{VRX}| + (k_3 + 1) \cdot \Delta_0\right]$$
$$+ \tan(\theta_t) \cdot (k_1 + k_2 + 2) \cdot \Delta_{up} = x_{RX} - x_{TX} \tag{A12}$$

Equation (12) clearly coincides with Eq. (13). By repeating the same procedure, evidence of Eqs. (14) – (16) can be then straightforwardly achieved.

APPENDIX B

Let's consider a ray connecting the TX and the RX through m reflections and two refractions. In order that it doesn't get lost in the top/bottom layer, the number of reflections in the upper/lower layer (k in Fig. 3) must be odd in the range [1÷m]. Therefore, the ray can be identified by the sequence of characters $' \underbrace{rr..rrt\overbrace{rr...rr}^{k}trr..rr}_{m+2}'$. The overall number of rays compliant with such representation can be computed as the permutations of $(m - k + 1)$ elements, where the element 'r' recurs $(m - k)$ times and the element $t\overbrace{rr...rr}^{k}t$ only once, i.e.:

$$P(m, k) = \frac{(m - k + 1)!}{(m - k)!} = m - k + 1 \tag{B1}$$

As already outlined, the same string actually corresponds to a pair of rays, the former having the first reflection on the upper interface, the latter on the lower one. Therefore, the number of rays in the previously defined class RmT2 can be expressed as:

$$N_{RmT2} = N_{RmT2}^{UP} + N_{RmT2}^{DOWN} \tag{B2}$$

$$N_{RmT2}^{UP} = N_{RmT2}^{DOWN} = \sum_{k=1, k\,odd}^{m} P(m, k)$$

$$= \sum_{k=1, k\,odd}^{m} (m - k + 1), \quad m \geq 1 \tag{B3}$$

Similar considerations can be repeated for the *m*-reflected, fourfold refracted rays. According to Fig. 4, each ray belonging to the class RmT4 can be associated with the string $' \underbrace{rr...rrt\overbrace{rr...rr}^{k_1}t\overbrace{rr...rr}^{k_3}t\overbrace{rr...rr}^{k_2}trr...rr}_{m+4}'$. As already discussed, k_1 and k_2 must be odd in order that the ray can come back to the antenna layer and finally reach the RX. Conversely, k_3 can be either even or odd. In the former case, the ray propagate in both the upper and the lower layer, whereas the four refraction occurs across the same interface in the latter. The total number of rays corresponding to the previous

sequence is therefore equal to the permutations of $(m-k_1-k_2-k_3+1)$ elements, where the element 'r' recurs $(m-k_1-k_2-k_3)$ times and the element $'t\overbrace{rr...rr}^{k_1}t\overbrace{rr...rr}^{k_3}t\overbrace{rr...rr}^{k_2}t'$ just once, i.e.:

$$P(m, k_1, k_2, k_3) = \frac{(m - k_1 - k_2 - k_3 + 1)!}{(m - k_1 - k_2 - k_3)!}$$
$$= m - k_1 - k_2 - k_3 + 1 \quad (B4)$$

Therefore, the number of rays fourfold refracting through the upper interface (N_{RmT4}^{UP}) or through the lower one (N_{RmT4}^{DOWN}) is equal to:

$$N_{RmT4}^{UP} = \sum_{k_1=1,odd}^{m-2} \sum_{k_2=1,odd}^{m-k_1-1} \sum_{k_3=1,odd}^{m-k_1-k_2} m - k_1 - k_2 - k_3 + 1,$$
$$m \geq 3$$
$$N_{RmT4}^{DOWN} = N_{RmT4}^{UP} \quad (B5)$$

Similarly, the following expression holds for the number of rays with refraction first into the upper layer and then into the lower one $(N_{RmT4}^{UP-DOWN})$, as well as for the rays firstly refracting into the lower layer and then into the upper one $(N_{RmT4}^{DOWN-UP})$:

$$N_{RmT4}^{UP-DOWN} = \sum_{k_1=1,odd}^{m-1} \sum_{k_2=1,odd}^{m-k_1} \sum_{k_3=0,even}^{m-k_1-k_2} m - k_1 - k_2 - k_3 + 1,$$
$$m \geq 2$$
$$N_{RmT4}^{DOWN-UP} = N_{RmT4}^{UP-DOWN} \quad (B6)$$

Finally, the cardinality of the class RmT4 can be computed as:

$$N_{RmT4} = N_{RmT4}^{UP} + N_{RmT4}^{DOWN} + N_{RmT4}^{UP-DOWN} + N_{RmT4}^{DOWN-UP}. \quad (B7)$$

APPENDIX C

Fig. 6 shows a dielectric slab with thickness d illuminated by an electromagnetic wave impinging from an angle of incidence θ_{inc}. Let the wave be uniform and plane for the sake of simplicity, and the materials homogeneous, isotropic and lossless. The total back-scattered field is the result of the direct reflection from the outer interface (dashed-dotted line in Fig. 6), plus the contributions undergoing multiple reflections inside the slab (continuous and dashed lines in Fig. 6). The field immediately reflected at the left boundary can be related to the incident field through the Fresnel reflection coefficient from medium 1 to medium 2 (R_{12}), i.e.:

$$\overrightarrow{E}_1 = R_{12} \cdot \overrightarrow{E}_{inc} \quad (C1)$$

The field carried by the ray penetrating the slab and experiencing one reflection at the right interface (continuous line in Fig. 6) can be instead expressed as:

$$\overrightarrow{E}_2 = T_{12} \cdot R_{23} \cdot T_{21} \cdot e^{j\beta\Delta} \cdot e^{-j\beta'2\ell} \cdot \overrightarrow{E}_{inc} \quad (C2)$$

being R_{23} the reflection coefficient from medium 2 to medium 3, T_{12} and T_{21} the transmission coefficient in and

from medium 2, β and β' the wave numbers in medium 1 and medium 2, Δ and ℓ as explained in Fig. 6. It can be noted that the factors $P_a = \exp(j\beta\Delta) = \exp(j2\beta\ell\sin\theta_i \cdot \sin\theta_t]$ and $P_d = \exp(-2j\beta'\ell)$ respectively accounts for the phase difference in the incident impinging fields and the phase shift introduced by propagation inside the slab. Adding up all the field contributions leads to the following expression:

$$\overrightarrow{E}_{tot} = \left[R_{12} + T_{12} \cdot T_{21} \cdot \sum_{n=2}^{\infty} (R_{23})^{n-1} \cdot (R_{21})^{n-2} \right.$$
$$\left. \times (P_d)^{2n-2} \cdot (P_a)^{n-1} R_{23} \right] \cdot \overrightarrow{E}_{inc}$$

$$\overrightarrow{E}_{tot} = \left[R_{12} + T_{12} \cdot T_{21} \cdot (R_{21})^{-1} \right.$$
$$\left. \times \sum_{n=2}^{\infty} \left(R_{23} \cdot R_{21} \cdot P_d^2 \cdot P_a \right)^{n-1} \right] \cdot \overrightarrow{E}_{inc} \quad (C3)$$

As $|R_{23} \cdot R_{21} \cdot P_d^2 \cdot P_a| < 1$, the geometric series can be re-written in closed form as:

$$\sum_{n=2}^{\infty} \left(R_{23} \cdot R_{21} \cdot P_d^2 \cdot P_a \right)^{n-1} = \frac{R_{23} \cdot R_{21} \cdot P_d^2 \cdot P_a}{1 - R_{23} \cdot R_{21} \cdot P_d^2 \cdot P_a} \quad (C4)$$

Since $R_{21} = -R_{12}$, then:

$$\overrightarrow{E}_{tot} = \left[R_{12} - \frac{T_{12} \cdot T_{21}}{R_{12}} \cdot \frac{-R_{23} \cdot R_{12} \cdot P_d^2 \cdot P_a}{1 + R_{23} \cdot R_{12} \cdot P_d^2 \cdot P_a} \right] \cdot \overrightarrow{E}_{inc}$$
$$\overrightarrow{E}_{tot} = \left[R_{12} + \frac{T_{12} \cdot T_{21}}{R_{12}} \cdot \frac{R_{23} \cdot R_{12} \cdot P_d^2 \cdot P_a}{1 + R_{23} \cdot R_{12} \cdot P_d^2 \cdot P_a} \right] \cdot \overrightarrow{E}_{inc}$$
$$(C5)$$

The complex term relating $\overrightarrow{E}_{inc}$ to $\overrightarrow{E}_{tot}$ can be regarded as the enhanced reflection coefficient, i.e.:

$$R_{en} = R_{12} + \frac{T_{12} \cdot T_{21}}{R_{12}} \cdot \frac{R_{23} \cdot R_{12} \cdot P_d^2 \cdot P_a}{1 + R_{23} \cdot R_{12} \cdot P_d^2 \cdot P_a}. \quad (C6)$$

REFERENCES

[1] X. Timoneda *et al.*, "Engineer the channel and adapt to it: Enabling wireless intra-chip communication," *IEEE Trans. Commun.*, vol. 68, no. 5, pp. 3247–3258, May 2020, doi: 10.1109/TCOMM.2020.2973988.

[2] F. Fuschini *et al.*, "Ray tracing modeling of electromagnetic propagation for on-chip wireless optical communications," *J. Low Power Electron. Appl.*, vol. 8, no. 4, p. 39, 2018.

[3] P. Van Zant, *Microchip Fabrication: A Practical Guide to Semiconductor Process*. New York, NY, USA: McGraw-Hill Educ., 2014;

[4] S. Abadal, C. Han, and J. M. Jornet, "Wave propagation and channel modeling in chip-scale wireless communications: A survey from millimeter-wave to terahertz and optics," *IEEE Access*, vol. 8, pp. 278–293, 2020, doi: 10.1109/ACCESS.2019.2961849.

[5] M. Nafari, L. Feng, and J. M. Jornet, "On-chip wireless optical channel modeling for massive multi-core computing architectures," in *Proc. IEEE Wireless Commun. Netw. Conf. (WCNC)*, 2017, pp. 1–6, doi: 10.1109/WCNC.2017.7925962.

[6] J. Fu, P. Juyal, and A. Zajić, "Modeling of 300 GHz chip-to-chip wireless channels in metal enclosures," *IEEE Trans. Wireless Commun.*, vol. 19, no. 5, pp. 3214–3227, May 2020, doi: 10.1109/TWC.2020.2971206.

[7] Y. Chen and C. Han, "Channel modeling and characterization for wireless networks-on-chip communications in the millimeter wave and terahertz bands," *IEEE Trans. Mol. Biol. Multi-Scale Commun.*, vol. 5, no. 1, pp. 30–43, Oct. 2019, doi: 10.1109/TMBMC.2019.2952863.

[8] L. Yan and G. W. Hanson, "Wave propagation mechanisms for intra-chip communications," *IEEE Trans. Antennas Propag.*, vol. 57, no. 9, pp. 2715–2724, Sep. 2009, doi: 10.1109/TAP.2009.2027158.

[9] A. N. Sommerfeld, "Propagation of waves in wireless telegraphy," *Ann. Phys.*, vol. 333, no. 4, pp. 665–737, 1909.

[10] J. R. Wait, "Fundamentals of mode theory of wave propagation," in *Electromagnetic Waves in Stratified Media*, vol. 3. Oxford, U.K.: Pergamon, 2013.

[11] H. R. Zeng, T. He, and K. Li, "Mode theory and propagation of ELF radio wave in a multilayered oceanic lithosphere waveguide," *IEEE Trans. Antennas Propag Propag.*, vol. 69, no. 9, pp. 5870–5880, Sep. 2021, doi: 10.1109/TAP.2021.3060902.

[12] D. K. N. da Silva, L. E. C. Eras, A. A. Moreira, L. M. Correia, F. J. B. Barros, and G. P. dos Santos Cavalcante, "A propagation model for mixed paths using dyadic green's functions: A case study over the river for a city–river–forest path," *IEEE Antennas Wireless Propag. Lett.*, vol. 17, pp. 2364–2368, 2018, doi: 10.1109/LAWP.2018.2875333.

[13] M.H. Cho and W. Cai, "Efficient and accurate computation of electric field dyadic green's function in layered media," *J. Sci. Comput.*, vol 71, no. 3, pp. 1319–1350, Jun. 2017, doi: 10.1007/s10915-016-0341-3.

[14] C. Mineo, D. Lines, and D. Cerniglia, "Generalised bisection method for optimum ultrasonic ray tracing and focusing in multi-layered structures," *Ultrasonics*, vol. 111, Mar. 2021, Art. no. 106330, doi: 10.1016/j.ultras.2020.106330.

[15] X.-P. Tang and C.-Y. Bai "Multiple ray tracing within 3-D layered media with the shortest path method," *Chin. J. Geophys.*, vol. 52, no. 5, pp. 1130–1138, Sep. 2009, doi: 10.1002/cjg2.1438.

[16] Y. Tian, D. Zhou, S. Kong, W. Zhang, B. Li, and J. Qi, "Modeling and simulation on three-layer media propagation characteristics of underwater electromagnetic field in shallow sea area" in *Proc. IAEAC*, Chengdu, China, 2019, pp. 1515–1518, doi: 10.1109/IAEAC47372.2019.8997918.

[17] C. Yeh, "Book reviews—Dyadic green's functions in electromagnetic theory," *IEEE Antennas Propag. Group Newslett.*, vol. 14, no. 3, p. 7, Sep. 1972, doi: 10.1109/MAP.1972.27131.

[18] W. Cai and T. Yu, "Fast Calculations of dyadic green's functions for electromagnetic scattering in a multilayered medium," *J. Comput. Phys.*, vol. 165, no. 1, pp. 1–21, Nov. 2000, doi: 10.1006/jcph.2000.6583.

[19] G. W. Hanson, "Dyadic green's function for a multilayered planar medium—A dyadic eigenfunction approach," *IEEE Trans. Antennas Propag.*, vol. 52, no. 12, pp. 3350–3356, Dec. 2004, doi: 10.1109/TAP.2004.836409.

[20] L.-W. Li, J.-H. Koh, T.-S. Yeo, M.-S. Leong, and P.-S. Kooi, "Analysis of radiowave propagation in a four-layered anisotropic forest environment," *IEEE Trans. Geosci. Remote Sens.*, vol. 37, no. 4, pp. 1967–1979, Jul. 1999, doi: 10.1109/36.774708.

[21] D. Liao and K. Sarabandi, "Near-Earth wave propagation characteristics of electric dipole in presence of vegetation or snow layer," *IEEE Trans. Antennas Propag.*, vol. 53, no. 11, pp. 3747–3756, Nov. 2005, doi: 10.1109/TAP.2005.856347.

[22] F. Fuschini *et al.*, "Ray tracing channel modeling for optical wireless networks on-chip," in *Proc. 15th EuCAP*, 2021, pp. 1–5.

[23] C. A. Balanis, *Antenna Theory*, 2nd ed. New York, NY, USA: Wiley, 1997.

[24] H. L. Bertoni, *Wireless Propagation for Modern Wireless Systems*, 1st ed. Hoboken, NJ, USA: Prentice Hall PTR, 2000;

[25] W. Burnside and K. Burgener, "High frequency scattering by a thin lossless dielectric slab," *IEEE Trans. Antennas Propag.*, vol. 31, no. 1, pp. 104–110, Jan. 1983, doi: 10.1109/TAP.1983.1143019.

[26] J. Nanni *et al.*, "Multi-path propagation in on-chip optical wireless links," *IEEE Photon. Technol. Lett.*, vol. 32, no. 17, pp. 1101–1104, Sep. 1, 2020, doi: 10.1109/LPT.2020.3012877.

[27] C. Garcia-Meca *et al.*, "On-chip wireless silicon photonics: From reconfigurable interconnects to lab-on-chip devices," *Light Sci. Appl.*, vol. 6, no. 9, Sep. 2017, Art. no. e17053. [Online]. Available: https://doi.org/10.1038/lsa.2017.53

[28] A. Biberman *et al.*, "Photonic network-on-chip architectures using multilayer deposited silicon materials for high-performance chip multiprocessors" *ACM J. Emerg. Technol. Comput. Syst.*, vol. 7, no. 2, p. 7, Jul. 2011, doi: 10.1145/1970406.1970409.

[29] D. Jiles, *Introduction to the Electronic Properties of Materials*. Cheltenham, U.K.: Nelson Thornes, 1994.

[30] D. Didascalou, J. Maurer, and W. Wiesbeck, "Subway tunnel guided electromagnetic wave propagation at mobile communications frequency," *IEEE Trans. Antennas Propag.*, vol. 49, no. 11, pp. 1590–1596, Nov. 2001, doi: 10.1109/8.964095.

[31] J. S. Lu *et al.*, "A discrete environment-driven GPU-based ray launching algorithm," *IEEE Trans. Antennas Propag.*, vol. 67, no. 2, pp. 1180–1192, Feb. 2019, doi: 10.1109/TAP.2018.2880036.

FRANCO FUSCHINI received the M.Sc. degree in telecommunication engineering and the Ph.D. degree in electronics and computer science from the University of Bologna in March 1999 and in July 2003, respectively, where he is currently an Associate Professor with the Department of Electrical, Electronic and Information Engineering "G. Marconi." He has authored or coauthored more than 30 journal papers on radio propagation and wireless system design. His main research interests are in the area of radio systems design and radio propagation channel theoretical modeling and experimental investigation. In April 1999, he was a recipient of the Marconi Foundation Young Scientist Prize in the context of the XXV Marconi International Fellowship Award.

MARINA BARBIROLI received the Laurea degree in electronic engineering and the Ph.D. degree in computer science and electronic engineering from the University of Bologna in 1995 and 2000, respectively.

Since 2020, she has been an Associate Professor with the University of Bologna. The research activity includes the participation to European research and cooperation programs (COST 259, COST 273 COST2100, COST IC004, and COST IRACON) and in the European Networks of Excellence FP6-NEWCOM and FP7-NEWCOM++. Her research interests are on propagation models for mobile communications systems, with focus on wideband channel modeling for 5G systems. Research activities includes investigation of planning strategies for mobile systems, broadcast systems and broadband wireless access systems, analysis of exposure levels generates by all wireless systems, and for increasing spectrum efficiency.

GAETANO BELLANCA received the M.Sc. degree in electronic engineering and the Ph.D. degree in electronic and computer science from the University of Bologna in 1991 and 1995, respectively. He joined the Department of Engineering, University of Ferrara in 1999, where he is currently an Associate Professor of Electromagnetics. His main research interests are in the design and characterization of optical components and devices and in the development of numerical techniques for electromagnetics in the fields of applied microwave, antennas, and integrated optics.

GIOVANNA CALÒ (Member, IEEE) received the master's degree in electronic engineering and the Ph.D. degree in electromagnetism from the Polytechnic University of Bari, Bari, Italy, in 2002 and 2006, respectively.

She joined the Department of Electrical and Electronic Engineering, Polytechnic University of Bari in 2002, where she is currently an Associate Professor of Electromagnetism. Her main research interests are computational electromagnetics, on-chip optical interconnections, integrated plasmonic nanoantennas for wireless on-chip optical communications, photonic crystals, plasmonic nanostructures, and components.

JACOPO NANNI received the B.Sc. and M.Sc. degrees in telecommunications engineering from the University of Bologna, Italy, in October 2012 and March 2015, respectively, and the double Ph.D. degrees from the University of Bologna, and Université Paris-Est, ESYCOM, ESIEE Paris, Noisy-le-Grand, France, in December 2018 working on low cost and low consumption Radio-over-Fiber (RoF) systems based on Vertical Cavity Surface Emitting Lasers for indoor applications. In July 2021, he Joined the Department of Electrical, Electronic and Information Engineering "Guglielmo Marconi," University of Bologna as a Research Associate. He is currently working on RoF systems for efficient cellular network infrastructures and in the field of radioastronomy within the Square Kilometer Array Project. Moreover, part of his work is dedicated to the study of optical wireless networks on-chip and the optimization of low-cost optical coupling structures.

VINCENZO PETRUZZELLI was born in 1955, in Bari, Italy. He received the graduate degree in electrical engineering from the University of Bari, Bari, in 1986. He is currently engaged as an Associate Professor of Electromagnetic Fields with the Department of Electrical and Electronic Engineering, Polytechnic University of Bari. He is a member of Electronic Engineer Doctorate Courses. He has coauthored over 330 publications, 132 of which published on international journals and 155 presented at international conferences. Over the years he has dealt with various research topics: integrated plasmonic nanoantennas for wireless on-chip optical communications; innovative optical devices for the optical interconnects on chip; periodic structures for laser cavities based on the optical self-collimation property of mesoscopic structures; plasmonic periodic nanostructures for the realization of plasmonic sensors. He acts as a reviewer of European and national projects. He was a member of the Management Committee of the MP0805 COST Action "Novel Gain Materials and Devices Based on III-V-N Compounds."